



High filling alumina/epoxy nanocomposite as coating layer for Fe-based amorphous powder cores with enhanced magnetic performance

Yiqun Zhang^{1,2} · Yaqiang Dong^{1,2} · Lei Liu¹ · Liang Chang¹ · Bang Zhou¹ · Qiang Chi¹ · Xinmin Wang¹

Received: 9 April 2019 / Accepted: 9 July 2019 / Published online: 15 July 2019
© Springer Science+Business Media, LLC, part of Springer Nature 2019

Abstract

A high-filling alumina/epoxy nanocomposite with improved thermal stability and insulation performance has been successfully designed as an organic–inorganic coating layer for the toroid-shaped FeSiBPNbCr amorphous magnetic powder cores (AMPCs). Unlike the organic coating, the organic–inorganic hybrid coating cores exhibited superior magnetic properties without compromising on saturation magnetization and permeability. The core loss declined by 40%, and the quality factor was 13% higher as half alumina was introduced into the epoxy resin matrix. A thin and uniform-coating layer of alumina/epoxy nanocomposite led to better high-frequency characteristics than those obtained with direct coating of the cores with alumina. Besides the outstanding magnetic properties, the Fe-based AMPCs with a convenient insulation-coating process cost lesser than Fe–Ni magnetic powder cores, thereby rendering the Fe-based AMPCs a potential candidate for a variety of industrial applications.

1 Introduction

Soft magnetic composites (SMCs) containing magnetic powders surrounded by insulation coatings promise revolutionized designs of electromagnetic devices to improve efficiency and reduce weight and costs, without compromising magnetic performance [1–5]. Unlike traditional magnetic materials, such as pure Fe, Fe–Si, Fe–Ni, Fe–Ni–Mo, and Fe–Si–Al, the Fe-based amorphous alloys exhibit high resistivity and low coercivity [6, 7]; as a result, Fe-based amorphous magnetic powder cores (AMPCs) have the advantages of 3D isotropic magnetic fields, high saturation induction, high permeability under a DC magnetic bias field, high resistivity, relatively low core loss, and flexibility of design [8–11]. Nevertheless, the permeability of Fe-based AMPCs is relatively low, and it is not advisable to compromise on

their permeability by introducing excessive nonmagnetic materials to reduce core loss. Therefore, an appropriate coating layer is crucial for Fe-based AMPCs to achieve higher permeability.

In high-frequency applications, the coating layer is critical to increase the electrical resistivity and achieve low core loss for AMPCs [5]. Besides the high electrical resistivity, satisfactory cohesiveness and thermal stability are also highly desirable for the coating layer to provide sufficient mechanical strength and to make high-temperature annealing possible for stress relaxation. Organic polymers, usually epoxy [12], silicone [13], polyimide [14], phenolic [15], and hybrids of these [16], can create an embedded matrix on the surface of the powders. However, the thermal stability of the polymers is usually poor, which limits the annealing temperature of the cores. Inorganic materials, such as phosphates [17], oxides [18, 19], water glass [8], and ferrite [20–24], can form an encapsulation around each particle. However, additional lubricant is required to decrease the hysteresis loss (P_h), which reduces the magnetic volume fraction and permeability [25]. Recently, microparticle/polymer or nanoparticle/polymer composites have been used as coating layers for SMCs. For example, SiO₂, ZnSO₄, and Fe₃O₄ have been mixed with phenol–formaldehyde resin and epoxy-modified silicone resin as a coating layer for pure Fe SMCs [26–29]. The hybrid coating layer results in a defect-free

✉ Yaqiang Dong
dongyq@nimte.ac.cn

¹ Zhejiang Province Key Laboratory of Magnetic Materials and Application Technology, CAS Key Laboratory of Magnetic Materials and Devices, Ningbo Institute of Materials Technology & Engineering, Chinese Academy of Sciences, Ningbo, Zhejiang 315201, China

² University of Chinese Academy of Sciences, Beijing 100049, China

structure of prepared green compacts, which consequently exhibit lower eddy current losses.

Furthermore, alumina nanoparticles have been coated around pure Fe powders directly before being treated with organic resin [30, 31]. However, the coating layer is not uniform, which introduces more pores and defects and then drastically reduces the permeability. To obtain a uniform coating layer, in this work, a high-filling alumina/epoxy nanocomposite has been designed as a coating layer for Fe-based AMPCs. Alumina nanoparticles were embedded into the epoxy resin matrix through a convenient mixing process, and the contents and effect of the alumina hybrid nanocomposite on the magnetic properties and microstructure of the Fe-based AMPCs were investigated systematically.

2 Experimental methods

2.1 Synthesis of FeSiBPnCr amorphous powders

Multicomponent alloy ingots with a nominal composition of $\text{Fe}_{77}\text{Si}_4\text{B}_{10}\text{P}_6\text{Nb}_2\text{Cr}_1$ were prepared by induction melting mixtures of industrial raw materials of pure Fe, Si, and Cr, pre-melted Fe–P, Fe–B, and Fe–Nb ingots in a pure argon atmosphere. Metallic powders with a fully amorphous phase were prepared by water atomization with a water pressure of 60 MPa.

2.2 Preparation of alumina/epoxy nanocomposite as the coating layer of the Fe-based amorphous powders

Al_2O_3 nanoparticles (≤ 20 nm, 99.99%, Aladdin Industrial Co.) were modified by 3-triethoxysilypropylamine (APTES, 99 wt%, Aladdin Industrial Co.) in ethanol for 0.5 h through ultrasonic dispersion. The modified nanoparticles were then introduced into epoxy resin dissolved in acetone. The mixture was treated by an ultrasonic dual-mixing process (UDM) of using ultrasonic vibration along with mechanical stirring by an impeller for 2 h at 50 °C. The amorphous powders were then uniformly mixed with 2 wt% nanocomposite by UDM until complete evaporation of the solvent occurred. The contents of the alumina in the nanocomposite were varied as 0, 10, 20, 30, 40, and 50 wt%. Accordingly, the powders coated by various alumina/epoxy nanocomposite were denoted as P-C₀ to P-C₅, respectively. The modified nanoparticles were also mixed with amorphous powders directly by UDM in acetone before being coated with epoxy resin. The contents of alumina and epoxy resin were the same as in the nanocomposite. The corresponding powders were denoted as P-D₀ to P-D₅, respectively.

Toroidal Fe-based AMPCs with an outer diameter of 20.3 mm, an inner diameter of 12.7 mm, and a height of

5.5 mm ($\Phi 20.3 \times \varphi 12.7 \times 5.5$ mm) were prepared by compaction of the as-coated amorphous powders mixed with 0.5 wt% zinc stearates as lubricant via cold pressing. The mixtures were unidimensional, consolidated by a pressure-testing machine (Suns YAW-600) under a pressure of 1800 MPa and dwell time of 60 s to obtain the powder cores. For stress relaxation, the Fe-based AMPCs were annealed at 460 °C for 1 h in vacuum. Accordingly, the AMPCs coated with various alumina/epoxy nanocomposites were marked as AMPCs-C₀ to AMPCs-C₅. For comparison, the AMPCs coated with various alumina were marked as AMPCs-D₀ to AMPCs-D₅.

2.3 Characterization

X-ray diffraction (XRD) analysis with Cu $K\alpha$ radiation was used for phase identification of the amorphous powders with a scan speed of 5°/min. Fourier transform infrared (FTIR) spectra were recorded in the wave number range of 400 to 4000 cm^{-1} at room temperature to investigate the composition of the coating layer. The thermal behavior was determined using a thermo-gravimeter analyzer (TG) in nitrogen atmosphere. The surface morphology of the coating layer on the surface of amorphous powders was examined with a scanning electron microscopy (SEM) coupled with energy-dispersive X-ray spectroscopy (EDS). The saturation magnetization (M_s) was measured by a vibrating sample magnetometer. The resistivity of the AMPCs was investigated by a hipot tester (Chroma 19073) at 50 V. Permeability spectra of the AMPCs were measured by an impedance analyzer (Agilent 4294A) from 1 kHz to 110 MHz with the contact electrodes in two-terminal connection configuration. The core loss of the samples was measured by an AC B-H loop tracer, and the DC-bias performance was measured by an LCR meter with 50 turns of copper wire twined tightly around the cores.

3 Results and discussion

Figure 1 shows the XRD pattern of the water-atomized FeSiBPnCr powders. Mainly, a broad diffraction peak around $2\theta = 45^\circ$ in the XRD pattern can be observed. No distinct diffraction peaks of the crystalline phase were observed, suggesting that the powders were almost fully in the amorphous phase. The inset in Fig. 1 shows the surface morphology of the amorphous powders with a particle size of less than 23 μm . Smaller particles were spherical, whereas larger particles were ellipsoidal and flat with round edges, which is appropriate for forming consolidated powder cores with high density [6]. The spherical-like amorphous powders are easy to insulate and are compact compared with the

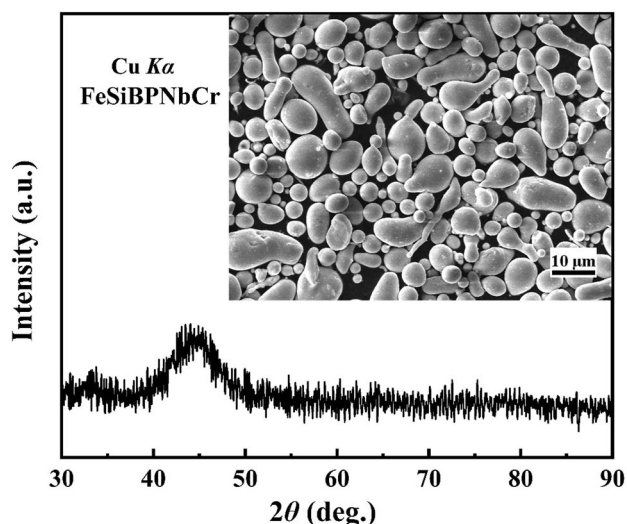


Fig. 1 XRD pattern of water-atomized FeSiBPnCr amorphous powders; the inset shows the morphology of the powders

ribbon breakage powders, which can reduce the interparticle eddy current loss of the powder cores.

To examine the surface chemistry structure of the nanocomposite, FTIR patterns of the FeSiBPnCr amorphous powders coated by various alumina/epoxy nanocomposites are shown in Fig. 2. The broad band around 3440 originates from $-\text{OH}$ groups of the absorbed water on the surface of the powders [32]. Some identical peaks can be seen in every sample, which are attributed to C-H stretching (2930 and 2870 cm^{-1}), aromatic C=C stretching (1608 cm^{-1}), COO^- stretching (1550 cm^{-1}), C-O-C stretching (1245 and 825 cm^{-1}), C-O stretching (1035 cm^{-1}), and $-\text{CF}_3$

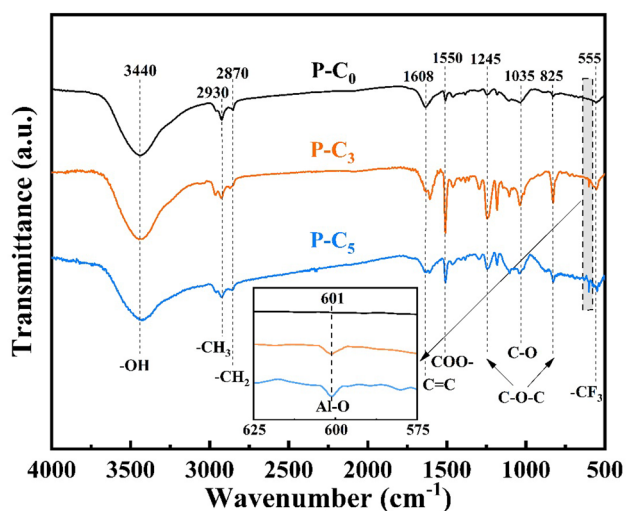


Fig. 2 FTIR patterns of the water-atomized FeSiBPnCr amorphous powders and powders coated by various alumina/epoxy nanocomposites

(555 cm^{-1}), originating from epoxy resin [33–36]. The weak peak near 601 cm^{-1} corresponds to the stretching vibration of Al-O in octahedral coordination [33], indicating that alumina nanoparticles were successfully coated around the surface of the amorphous powders. Comparing the curves of P-C₅ to P-C₃, the intensity of the peak increased, which was related to the higher alumina content.

The thermal stabilities of the water-atomized FeSiBPnCr amorphous powders and the powders coated with various alumina/epoxy nanocomposites were evaluated by using the TG technique at a heating rate of 10 °C/min in a nitrogen atmosphere, and the results are shown in Fig. 3. The weight of water-atomized powders remained constant up to 500 °C, whereas P-C₀ exhibited the lowest residual weight (98.2%), which means the epoxy completely decomposed. The residual weight increased as the content of alumina rose, indicating the high thermal stability of the alumina/epoxy nanocomposite. The high thermal stability of the alumina/epoxy nanocomposite is beneficial to the coating layer of the powders, which helps improve the frequency stability of permeability and reduce the core loss of the AMPCs. However, the P-C₅ revealed the largest weight loss below 330 °C. This may be due to evaporation of water adsorbed by nano alumina with a large specific surface area.

Figure 4 shows the SEM images, revealing the evolution of the surface morphologies of the FeSiBPnCr amorphous powders with different coating layers. The water-atomized FeSiBPnCr powders are clean and smooth, as shown in Fig. 4a, whereas some flocs are wrapped with ultra-micro-particles attached to the surface of P-C₀, which indicates that the powders were coated by a thick epoxy resin coating layer, as shown in Fig. 4b. Figures 4c and d show the

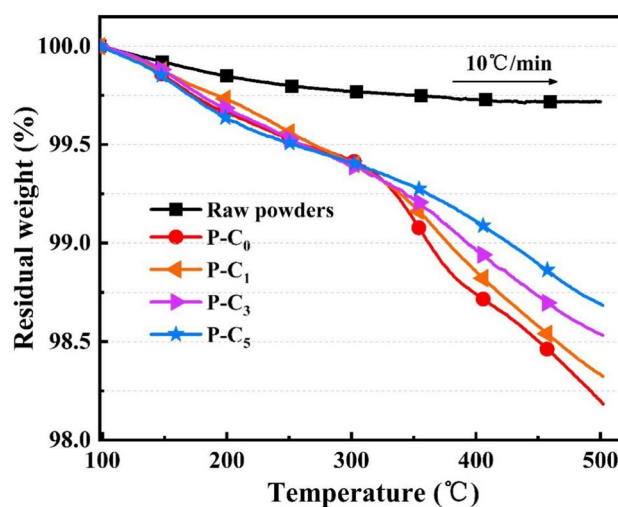


Fig. 3 TG curves of the water-atomized FeSiBPnCr amorphous powders and powders coated by various alumina/epoxy nanocomposites

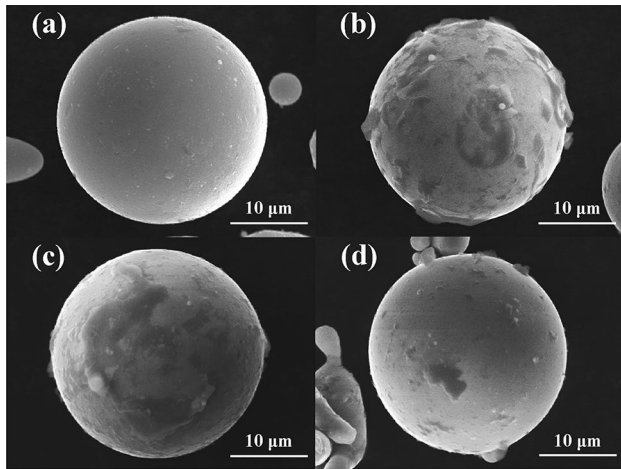


Fig. 4 SEM micrograph taken from the **a** water-atomized FeSiBPNbCr amorphous powders and **b** P-C₀, **c** P-C₃, and **d** P-C₅

surface morphologies of P-C₃ and P-C₅. With the increasing content of alumina, the surface of the powders is smoother and more uniform, which is attributed to the formation of a thinner coating, and this is crucial for fabricating AMPCs with excellent performances.

The elemental distribution maps of the FeSiBPNbCr amorphous powders coated by alumina/epoxy nanocomposite (P-C₅) and alumina (P-D₅) were acquired by EDS, as shown in Fig. 5. The elements, including Fe, Si, Nb, Cr, and Al, were evenly distributed on the surface of P-C₅ as shown in Fig. 5a. The EDS results of the cross section of AMPCs-C₅ after polishing are shown in Fig. 5b. It is clear that the Al element uniformly exists on the gap between the amorphous particles, which reveals that alumina nanoparticles have been evenly dispersed in the epoxy resin. Therefore, the EDS analysis demonstrates that the amorphous particles were coated by a uniform alumina/epoxy coating layer, and the nanoparticles and amorphous powders were well distributed. Alumina exhibited beneficial properties, such as a high melting point, thermal stability, and electrical resistivity, which are conducive to the improvement of comprehensive magnetic properties [32]. The Fe, Si, Nb, and Cr elements were also uniformly distributed around P-D₅; however, the Al element was gathered together, as shown in the circle in Fig. 5c. The alumina agglomerated together and nonuniformly distributed when the alumina connected to the particles directly by a coupling agent. This inhomogeneity deteriorates the insulation performance and soft magnetic performance.

Figure 6 shows the room temperature magnetization versus applied field curves of the FeSiBPNbCr amorphous powders and the powders coated with various alumina/epoxy nanocomposites. The presence of the epoxy resin coating layer reduced the M_s of the water-atomized

FeSiBPNbCr powders from 126 to 118 emu/g because of the lower weight fraction of the magnetic phases. The M_s values of the powders coated by different alumina/epoxy nanocomposites are about 118 emu/g. There was no appreciable distinction in the M_s values of samples with increasing content of alumina because of the fixed nonmagnetic weight value. This indicates that high-filling alumina/epoxy nanocomposite as a coating layer does not compromise the M_s for Fe-based amorphous powders.

The effective permeability (μ_e) as a function of the frequency for the AMPCs is shown in Fig. 7. All samples exhibited stable permeability at more than 1 MHz. The increased content of alumina nanoparticles in the epoxy resin led to a significant decrease in μ_e from 56 to 44 for AMPCs-C₀ to AMPCs-C₃. However, the μ_e then increased to 52 for alumina contents up to 50 wt%, as shown in Fig. 7a. The μ_e of AMPCs coated with alumina followed the same trend, as shown in Fig. 7b. The insulation material, which generally covers the surface of the magnetic powders, drastically deteriorated the μ_e [36]. The μ_e of the magnetic cores can be expressed as in Eq. (1) [17].

$$\mu_e = 1 + \frac{4\pi(\mu - 1)}{4\pi + N(\mu - 1)}(1 - p) \quad (1)$$

where μ is the intrinsic permeability of the material, N is the demagnetizing factor, and p is the volume fraction of nonmagnetic materials in the composites. The better insulation performance of alumina decreases the μ_e of the AMPCs. However, as the total mass of the nonmagnetic materials is constant, more alumina indicates a higher density and, thus, reduces the nonmagnetic volume fraction, leading to an increase in μ_e for the AMPCs with high-filling alumina/epoxy nanocomposite. A comparison of Figs. 7b and a shows that AMPCs-D₁ to AMPCs-D₅ exhibit lower μ_e than AMPCs-C₁ to AMPCs-C₅. The coating layer for the powders directly mixed with alumina is not uniform, which introduces more pores and defects and then drastically reduces the permeability.

The total core loss (P_{cv}), as an important magnetic performance index, is composed of P_h and eddy current loss (P_e) in power applications. P_h is proportional to frequency (f), whereas P_e varies with the square of f [37]. At low frequencies, the P_h is the major loss mechanism, and lower coercivity benefits the decrease of P_h . In the high-frequency range, the energy per cycle (P_{cv}/f) versus f curves show nearly linear behaviors, as shown in Fig. 8, indicating that P_e is the main source of loss. The P_e can be effectively reduced by appropriate insulation in the magnetic powders. Degradation of P_{cv} is mainly caused by the increased content of alumina in this work, as shown in Figs. 8c and d. Compared with AMPCs-C₀ (2730 mW/cm³), P_{cv} at 250 kHz dropped by 40% (1650 mW/cm³) as

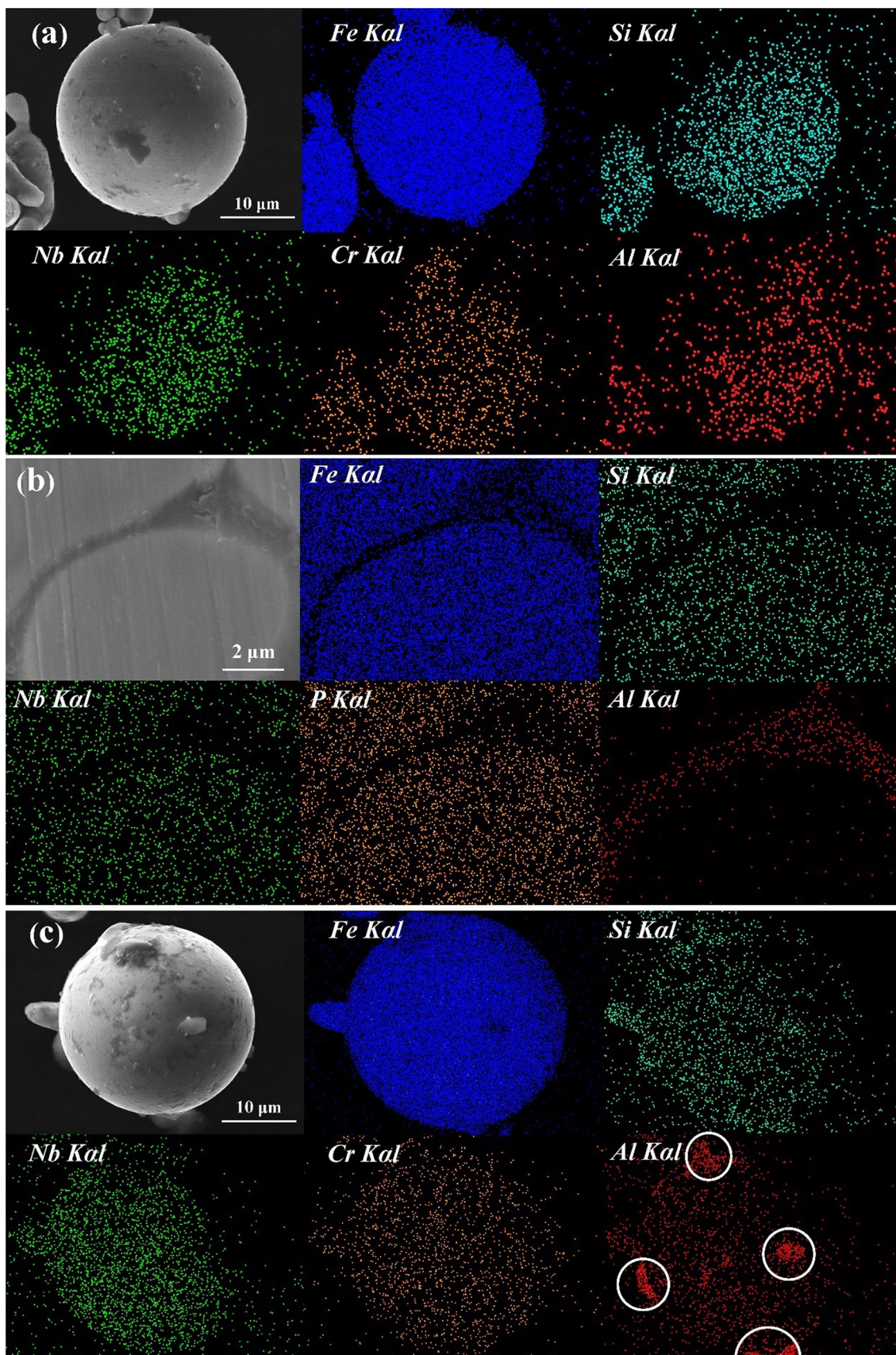


Fig. 5 SEM micrograph and EDS elemental distribution maps of **a** P-C₅, **b** cross-section of AMPCs-C₅ and **c** P-D₅

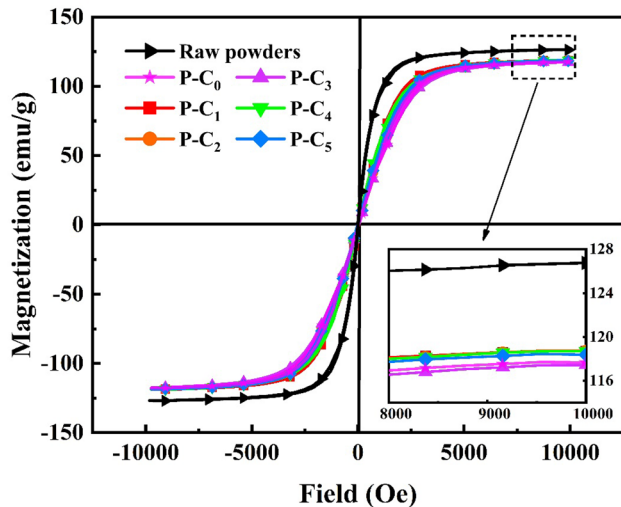


Fig. 6 M-H curves of the water-atomized FeSiBPNbCr amorphous powders and powders coated by various alumina/epoxy nanocomposites

the alumina content increased to 50 wt%. A decreased P_{cv} from 2710 to 2050 mW/cm³ was obtained for the AMPCs directly coated with increasing alumina content, from 10 to 50 wt%. For AMPCs, P_e consists of interparticle and intraparticle eddy current loss. The amorphous powders used for each sample were the same; therefore, the intraparticle eddy current loss can be regarded as similar. Interparticle eddy current loss can be expressed as Eq. (2) [38].

$$P_{inter} = \frac{\pi^2 d^2}{\beta \rho} B_m^2 f^2 \quad (2)$$

where d is the eddy current effective dimension, B_m is the maximum induction, β is the cross-section geometrical coefficient, and ρ is the resistivity. According to Eq. (3), for the sample with the same d and β , the P_{inter} is inversely proportional to the resistivity of the corresponding sample. Table 1 presents the electrical resistivity, density, and core loss of all the samples. The density remains constant, whereas the resistivity continuously increases with the increase in content of alumina. The high thermal stability and electrical resistivity of alumina lead to a better insulation capability for alumina/epoxy nanocomposite, which can sufficiently cut off the eddy current between the amorphous powders, resulting in the descending of P_{inter} and P_e .

For high-frequency applications, the amount of energy stored must be considered, as well as the losses. The quality factor (Q), as a crucial parameter, can be defined as Eq. (3) [39].

$$Q = \mu' / \mu'' \quad (3)$$

where μ' and μ'' are the real and imaginary parts of complex permeability, respectively. μ' is related to μ_e and the amount

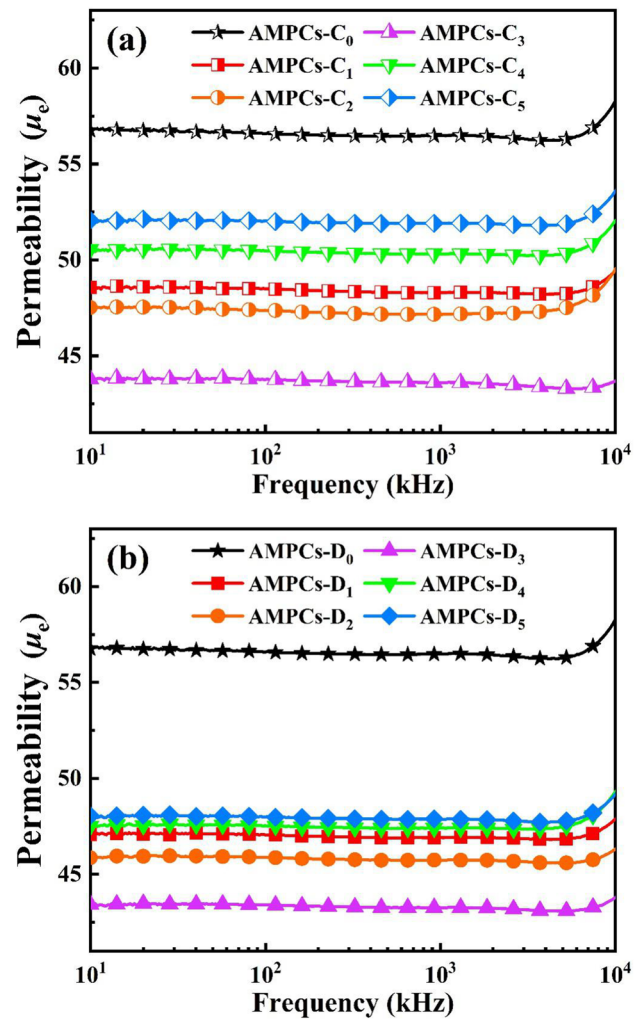


Fig. 7 Effective permeability (μ_e) of the AMPCs coated by a alumina/epoxy nanocomposite and b alumina

of energy stored, while μ'' is proportional to P_{cv} and can be defined as Eq. (4) [40].

$$P_{CV} = \pi f \mu_0 \mu'' H_m^2 \quad (4)$$

where f is the frequency of the varying magnetic field, μ_0 is vacuum permeability, and H_m is the magnetic field intensity. Therefore, combining Eqs. (3) and (4), the Q factor is inversely proportional to the P_{cv} :

$$Q = \pi f \mu_0 H_m^2 \mu' / P_{CV} \quad (5)$$

As shown in Figs. 9a and b, the Q factor rose first in the lower-frequency range peaked at a frequency of approximately 300 kHz, and then declined gradually with further increasing frequency. The high maximum level of the Q factor means the large amounts of power can be efficiently stored. The Q factor peaked at high frequency, indicating the excellent high-frequency characteristics of Fe-based AMPCs, which are much better than those of Fe–Ni SMCs

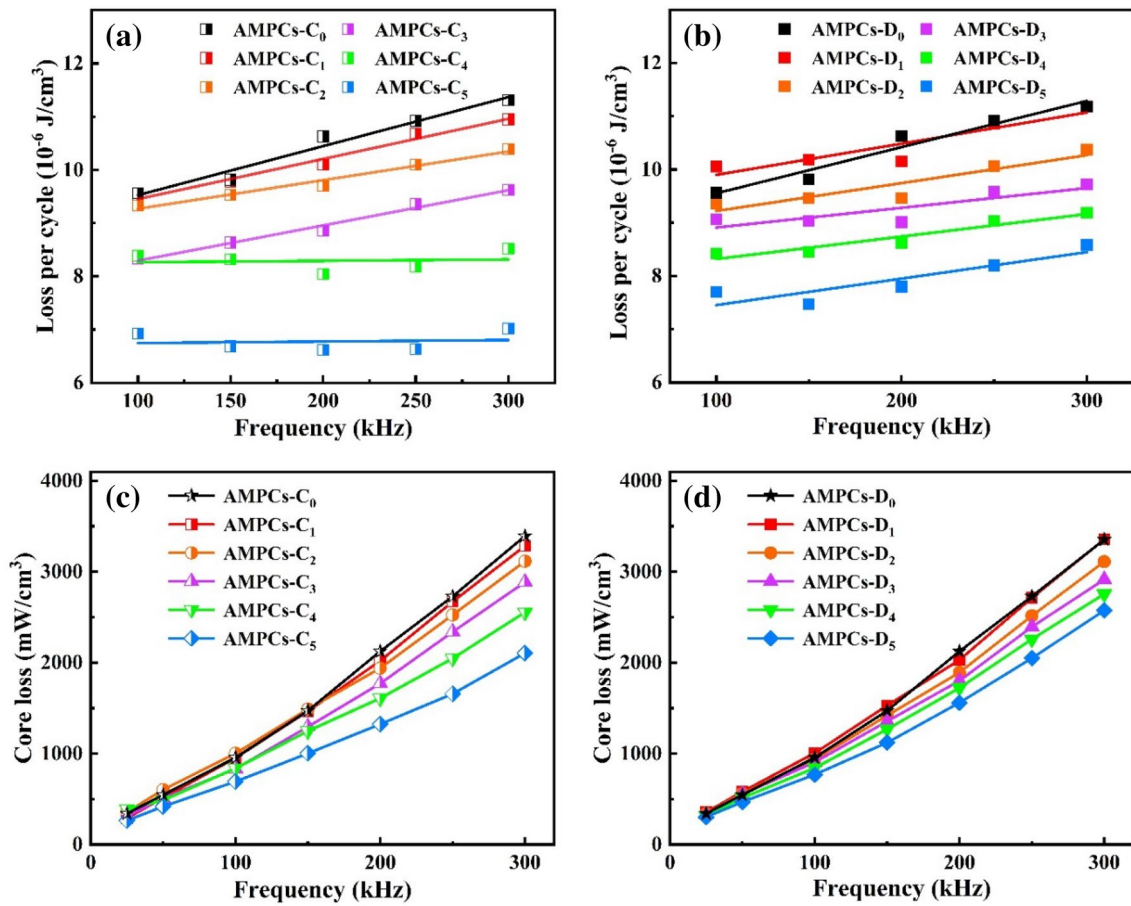


Fig. 8 Loss per cycle (P/f) and core loss (P_{cv}) of the AMPCs coated by (a) and (c) alumina/epoxy nanocomposite and (b) and (d) alumina

Table 1 Density, resistivity and core loss (P_{cv}) of the AMPCs coated by alumina/epoxy nanocomposite and alumina

Sample	Density (g/cm^3)	Resistivity ($\Omega\text{-cm}$)	P_{cv} (0.1T, 250kHz) (mW/cm^3)
AMPCs-C ₀	5.69	49	2730
AMPCs-C ₁	5.66	56	2670
AMPCs-C ₂	5.61	84	2520
AMPCs-C ₃	5.71	220	2280
AMPCs-C ₄	5.68	444	1940
AMPCs-C ₅	5.68	867	1650
AMPCs-D ₁	5.65	66	2710
AMPCs-D ₂	5.59	154	2520
AMPCs-D ₃	5.58	244	2390
AMPCs-D ₄	5.64	290	2260
AMPCs-D ₅	5.66	333	2050

(< 100 kHz) [1]. The Q factor was gently enhanced by the content of alumina in terms of its maximum value and the corresponding frequency. In detail, AMPCs-C₅ shows the maximum Q factor of 136 at a frequency of 324 kHz, which

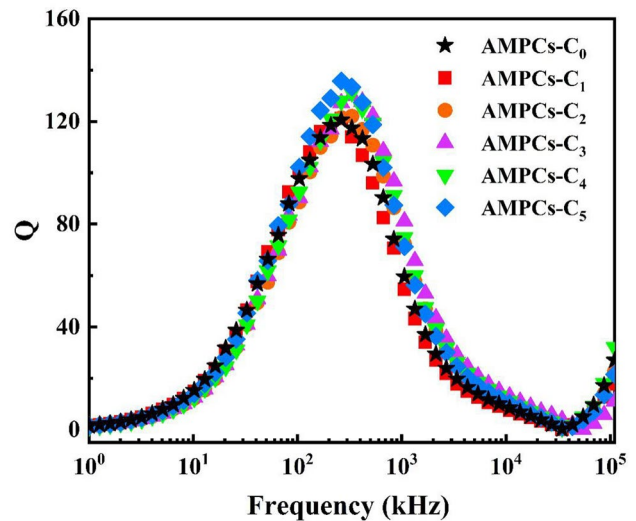


Fig. 9 The quality factor (Q) of the AMPCs coated by alumina/epoxy nanocomposite

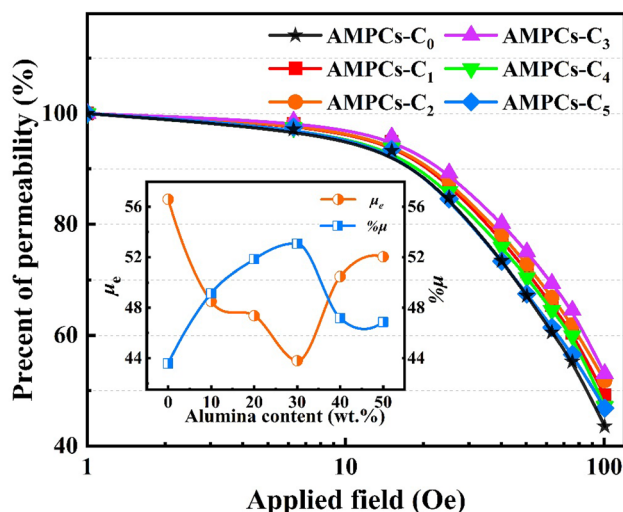


Fig. 10 The percentage of permeability ($\% \mu$) of the AMPCs coated by alumina/epoxy nanocomposite; the inset shows the variations in μ_e and $\% \mu$ for corresponding AMPCs

is 13% higher than that of AMPCs- C_0 (120). According to Eq. (4), a higher Q factor for AMPCs- C_5 indicates a lower P_{cv} and better soft magnetic properties at high frequency [12].

In recent years, an increasing number of magnetic components need to operate under DC-bias conditions to improve the power density of devices. The DC-bias field dependence of the percentage of permeability ($\% \mu$) is another important property for the AMPCs, and it is closely related to M_s and distributed air gaps. The results of $\% \mu$ at a frequency of 100 kHz are shown in Fig. 10, and AMPCs- C_3 and AMPCs- D_3 display the best performance at 100 Oe, which is 23% higher than that of the nonalumina AMPCs. Then, $\% \mu$ drops as μ_e increases, but the $\% \mu$ of AMPC- C_5 is still 9% higher than that of AMPC- C_0 . The inset in Fig. 10 presents the variations in μ_e and $\% \mu$ for AMPCs coated with different alumina content. The change in $\% \mu$ exactly follows the opposite trend of change in μ_e as alumina content increases. It indicates that the change of $\% \mu$ is closely related to μ_e . For SMCs with similar M_s and density, increasing μ_e can reduce the DC superposition characteristic, because the magnetic material saturates at a lower current [41].

4 Conclusions

A high-filling alumina/epoxy nanocomposite was successfully fabricated as the coating layer for FeSiBPNbCr AMPCs, and their microstructures and magnetic properties were investigated. The permeability of the corresponding AMPCs dropped at first and then increased as the amount of alumina increased, and the core loss kept declining

simultaneously. Compared with the AMPCs coated by a direct-mixing method, significant improvement in soft magnetic performance was also achieved with AMPCs coated with alumina/epoxy nanocomposites, owing to the thin and uniform alumina/epoxy nanocomposite coating layer. The AMPCs with 50% alumina embedded in the epoxy matrix displayed the lowest P_{cv} of 1650 mW/cm³ (measured at 0.1 T, 250 kHz), relatively high μ_e of 51, and good magnetic characteristics over a wide range of frequencies.

Acknowledgments This work was supported by the China International Cooperation Project (Grant No. 2016YFE0126700), S&T Innovation 2025 Major Special Program (Grant No. 2018B10062) and the National Natural Science Foundation of China (Grant No. 51601205).

References

- H. Shokrollahi, K. Janghorban, J. Mater. Process. Technol. **189**, 1–12 (2007)
- G. Herzer, Acta Mater. **61**, 718–734 (2013)
- D. Liu, C. Wu, M. Yan, J. Wang, Acta Mater. **146**, 294–303 (2018)
- E.A. Périgo, B. Weidenfeller, P. Kollár, J. Füzer, Appl. Phys. Rev. **5**, 031301 (2018)
- A.M. Leary, P.R. Ohodnicki, M.E. Henry, JOM **64**, 772–781 (2012)
- J.M. Silveira, E. Ferrara, D.L. Huber, T.C. Monson, Science **362**, 418 (2018)
- H. Chen, B.S. Dong, S.X. Zhou, X.X. Li, J.Y. Qin, Sci. Rep. **8**, 5680 (2018)
- M. Yagi, I. Endo, I. Otsuka, H. Yamamoto, R. Okuno, H. Koshimoto, A. Shintani, J. Magn. Magn. Mater. **215**, 284–287 (2000)
- H.P. Xu, R.W. Wang, D. Wei, C. Zeng, J. Magn. Magn. Mater. **385**, 326–330 (2015)
- I. Otsuka, T. Kadamura, K. Ishiyama, M. Yagi, IEEE Trans. Magn. **45**, 4294–4297 (2009)
- X.Y. Wang, C.W. Lu, F. Guo, Z.C. Lu, D.R. Li, S.X. Zhou, J. Magn. Magn. Mater. **324**, 2727–2730 (2012)
- X.X. Zhong, J.C. Chen, L. Wang, B.J. Li, L.Z. Li, J. Alloys Compd. **735**, 1603–1610 (2018)
- G.L. Zhao, C. Wu, M. Yan, J. Alloys Compd. **685**, 231–236 (2016)
- H.J. Kim, K.S. Kim, J.J. Song, S.C. Yoon, S.I. Kim, K.Y. Sohn, NSTI Nano. **1**, 581–583 (2011)
- A.H. Taghvaei, H. Shokrollahi, A. Ebrahimi, K. Janghorban, Mater. Chem. Phys. **116**, 247–253 (2009)
- M.M. Dias, H.J. Mozetic, J.S. Barboza, R.M. Martins, L. Pellegrini, L. Schaeffer, Pow. Tech. **237**, 213–220 (2013)
- Y.Y. Zheng, Y.G. Wang, G.T. Xia, J. Magn. Magn. Mater. **396**, 97–101 (2015)
- L.W. Qian, J.G. Peng, Z. Xiang, Y.F. Pan, W. Lu, J. Alloys Compd. **778**, 712–720 (2019)
- L. Huan, X.L. Tang, H. Su, H.W. Zhang, Y.L. Jing, J. Mater. Sci. **26**, 3275–3281 (2015)
- X. Peng, K. Peng, J.P. Huang, J. Alloys Compd. **691**, 165–170 (2017)
- X.L. Li, Y.Q. Dong, M. Liu, C.T. Chang, X.M. Wang, J. Alloys Compd. **696**, 1323–1328 (2017)
- S. Nakahara, E.A. Périgo, Y. Pittini, Y. Hazan, T. Graule, Acta Mater. **58**, 5695–5703 (2010)
- J.X. Li, J. Yu, W.C. Li, S.L. Che, J.W. Zheng, Q. Liang, Y. Yao, J. Magn. Magn. Mater. **454**, 103–109 (2018)

24. W.C. Li, W. Wang, J.J. Lv, Y. Ying, J. Yu, J.W. Zheng, Q. Liang, S.L. Che, *J. Magn. Magn. Mater.* **456**, 333–340 (2018)
25. J. Lei, J.W. Zheng, H.D. Zheng, L. Qiao, Y. Ying, W. Cai, *J. Magn. Magn. Mater.* **472**, 7–13 (2019)
26. M. Strečková, L. Medvecký, J. Füzér, P. Kollár, R. Bureš, M. Fáberová, *Mater. Lett.* **101**, 37–40 (2013)
27. M. Strečková, T. Sopčáka, L. Medvecký, R. Bureš, M. Fáberová, I. Batko, J. Briancin, *Chem. Eng. J.* **180**, 343–353 (2012)
28. C. Wu, M.Q. Huang, D.H. Luo, Y.Z. Jiang, M. Yan, *J. Alloys Compd.* **741**, 35–43 (2018)
29. D.H. Luo, C. Wu, M. Yan, *J. Magn. Magn. Mater.* **452**, 5–9 (2018)
30. Y.D. Peng, J.W. Nie, W.J. Zhang, J. Ma, C.X. Bao, Y. Cao, *J. Magn. Magn. Mater.* **399**, 88–93 (2016)
31. K.J. Sunday, K.A. Darling, F.G. Hanejko, B. Anasori, Y.C. Liu, M.L. Taheri, *J. Alloys Compd.* **653**, 61–68 (2015)
32. C. Wu, X.W. Gao, G.L. Zhao, Y.Z. Jiang, M. Yan, *J. Magn. Magn. Mater.* **452**, 114–119 (2018)
33. M.S. Goyat, S. Ray, P.K. Ghosh, *Compos. Part A* **42**, 1421–1431 (2011)
34. K. Szendrei, W. Gomulya, M. Yarema, W. Heiss, M.A. Loi, *Appl. Phys. Lett.* **97**, 115–119 (2010)
35. M. G. Jonzalez, J. C. Cabanelas, *Infra. Spec.* (2011)
36. Y. Pittini, E.A. Périgo, Y. Hazan, S. Nakahara, *Acta Mater.* **59**, 4291–4302 (2011)
37. T. Suzuki, P. Sharma, L. Jiang, Y. Zhang, A. Makino, *IEEE Trans. Magn.* **11**, 1–5 (2018)
38. W.C. Li, H.W. Cai, Y. Kang, Y. Ying, J.YuJW Zheng, Q. Liang, Y. Jiang, S.L. Che, *Acta Mater.* **167**, 267–274 (2019)
39. Y.W. Zhao, X.K. Zhang, J.Q. Xiao, *Adv. Mater.* **17**, 915–918 (2005)
40. C.D. Owens, *Proc. Ire.* **41**, 359–365 (1953)
41. L. Huan, X.L. Tang, H. Su, H.W. Zhang, Y.L. Jing, B.Y. Liu, *IEEE Trans. Magn.* **50**, 1–4 (2014)

Publisher's Note Springer Nature remains neutral with regard to jurisdictional claims in published maps and institutional affiliations.